Nano Research

Open Access

Research Article

Uniform $Ag_6Mo_{10}O_{33}$ meso/nanowires: High-efficient fabrication, novel growth mechanism, and reversibly high-energy sodium-ion battery

Yuqing Yang[1,§], Juan Liu[1,§], Meiqi Zhang[1,§], Qing Wang[1], Ziqing Gui[1], Xucheng Gu[1], Chunsheng Li[1,2]✉, Yan Sun[1,2]✉, Yuxuan Sun[1], Lianghuan Qin[1], Yuzhen Zhao[2]✉, Wanzheng Lu[3], Xiaofang Xu[4], and Xufeng Wang[5]

[1] *Key Laboratory of Advanced Electrode Materials for Novel Solar Cells for Petroleum and Chemical Industry of China, School of Chemistry and Life Sciences, Suzhou University of Science and Technology, Suzhou 215009, China*
[2] *Xi'an Key Laboratory of Advanced Photo-electronics Materials and Energy Conversion Device, School of Electronic Information, Xijing University, Xi'an 710123, China*
[3] *School of Safety Science and Engineering, Changzhou University, Changzhou 213164, China*
[4] *Suzhou Key Laboratory of Biophotonics, School of Optical and Electronic Information, Suzhou City University, Suzhou 215104, China*
[5] *State Key Laboratory of Advanced Chemical Power Sources, Guizhou Meiling Power Sources Co. Ltd, Zunyi 563003, China*
§ *Yuqing Yang, Juan Liu, and Meiqi Zhang contributed equally to this work.*

Cite this article: *Nano Research*, **2025**, *18*, 94907274. https://doi.org/10.26599/NR.2025.94907274

ABSTRACT: Silver molybdate ($Ag_6Mo_{10}O_{33}$) exhibits excellent catalytic properties and photocatalytic degradation owing to its unique chemical and structural characteristics, but its prospective applications in electrochemistry energy storage have not received sufficient attention. Herein, the $Ag_6Mo_{10}O_{33}$ meso/nanowires with superior morphological characteristics are fabricated employing a high-efficient microwave irradiation method. Furthermore, the novel synthesizing mechanism of ultralong $Ag_6Mo_{10}O_{33}$ mesowires is also proved to be a "self-assembly-dissolution-recrystallization-Ostwald-ripening" process, by exploring through the parallel experiments on the dramatic alterations in topology and size of $Ag_6Mo_{10}O_{33}$ at continuous reaction time. Additionally, the properties of the ultralong uniform $Ag_6Mo_{10}O_{33}$ mesowires for the sodium storage are investigated via cyclic voltammetry, electrochemical impedance spectroscopy and galvanostatic charge–discharge. Notably, these as-obtained $Ag_6Mo_{10}O_{33}$ mesowires exhibit an outstanding initial capacity (1587.9 mAh·g^{-1}), a remarkable specific capacity for the second cycle (817.9 mAh·g^{-1}), and an excellent reversible capacity (551.5 mAh·g^{-1} after 30 cycles). The superior electrochemical properties of the nanoscaled silver molybdate are ascribed to the lower charge transfer resistance due to the microstructure of the smallest size $Ag_6Mo_{10}O_{33}$ nanosheets that exhibit a thickness of around 5 nm, which can provide a great contact with the electrolyte, facilitating the rapid diffusion of sodium ions at the electrode/electrolyte interface and the rapid transport of sodium ions within the electrode materials. Thus, the proposed synthetic strategy and achieved deep insights will stimulate the development of $Ag_6Mo_{10}O_{33}$ for high-safety and long-life sodium ion batteries.

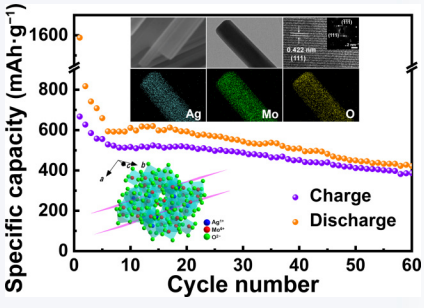

KEYWORDS: sodium-ion batteries, self-assembly-dissolution-recrystallization-Ostwald-ripening fabricating mechanism, microwave irradiation fabrication, $Ag_6Mo_{10}O_{33}$ meso/nanowires, energy storage and conversion

1 Introduction

To accommodate the dynamic advancement in energy storage systems and electric vehicle industries, there is an urgent requirement in rechargeable batteries with high capacity, dependable security and superior cycling performances [1–6]. Currently, sodium-ion batteries (SIBs) have garnered extensive attention in energy storage due to their advantages, such as high energy density, high safety, and abundant sodium resources [7–12]. However, the inherently large Na^+ radius (1.06 Å) typically leads to severe pulverization of electrode materials and sluggish transport dynamics in SIBs, resulting in the low reversible capacity and rapid capacity fade. Therefore, the search for advanced electrode materials has become urgent [13–17].

Received: December 20, 2024; **Revised:** January 25, 2025
Accepted: January 25, 2025

✉Address correspondence to Chunsheng Li, lichsheng@163.com; Yan Sun, juzi147@163.com; Yuzhen Zhao, zyz19870226@163.com

The anode materials for SIBs encompass conversion reaction materials such as transition metal oxides [18, 19], alloy/dealloying materials [20, 21], intercalation reaction materials [22, 23], and carbon-based materials [24, 25]. Recently, the metal molybdate oxides, a type of transition metal oxide, have emerged as important research areas in energy storage, owing to their stable composition, effective redox characteristics, and superior physicochemical traits [26, 27]. For example, Babu et al. presented an innovative $FeMoO_4$ anode material for SIBs, exhibiting an exceptional electrochemical performance with a specific capacity of 294 $mAh{\cdot}g^{-1}$ after 100 cycles at a current density of 50 $mA{\cdot}g^{-1}$, and the capacity retention maintaining approximately 100% after 1000 cycles at a current density of 0.5 $A{\cdot}g^{-1}$ [28]. Using a simple microwave irradiation method, Wang and co-workers created persimmon-like $CaMoO_4$ superstructures anchored on scattered mesocarbon microbeads (MCMB) powders. The materials produced demonstrated high initial capacity (991.3 $mAh{\cdot}g^{-1}$) and high-rate stability (84.9% retention even after 80th cycles) [29]. Among the diverse molybdate, $Ag_6Mo_{10}O_{33}$ features a layered structure that imparts distinctive physical and chemical properties, enabling it to exhibit exceptional efficacy in photocatalytic degradation, antimicrobial material synthesis, and catalytic reactions [30–32]. In terms of antibacterial activity, Moura et al. synthesized spinel-type cubic structure β-Ag_2MoO_4 microcrystals via the standard hydrothermal process, demonstrating antibacterial activity. The synthesized β-Ag_2MoO_4 particles exhibit clinically significant antibacterial properties and augment the efficacy of certain drugs against multidrug-resistant strains of *Staphylococcus aureus* and *Escherichia coli* [33]. Additionally, Daniela has created a controlled precipitation technique to synthesize extremely effective Ag_2MoO_4-based catalysts that can be used in various oxidation processes to degrade pantoprazole (PAN) in aqueous suspension [34].

However, research on silver molybdates in the field of electrochemical energy storage is relatively scarce, with scientists diligently working to uncover its energy storage potential and explore application prospects. In this context, the manufacture of silver molybdate electrode materials is particularly crucial. An important aspect of the research involves precisely controlling the morphological characteristics of the materials (including size, shape, and surface structure) to optimize their electrochemical performance [35–41]. The impressive electrochemical properties of these materials can be attributed to their unique microstructures, such as nanoscale dimensions and distinctive layered pore architectures, which provide numerous active sites and facilitate ion diffusion [42, 43]. Currently, the primary synthesis methods for silver molybdate nanomaterials encompass hydrothermal synthesis [44, 45], coprecipitation [34], solid-state reaction [46], and microwave-assisted technique [47]. Up to now, advancing microwave irradiation technology offers remarkable prospects for meso/nanomaterial synthesis via homogeneous liquid-phase fabrication, boasting high efficiency, speed, environmental sustainability, and selective heating [48–50]. Employing such advanced synthesis techniques, the microstructures of silver molybdate electrode materials can be tailored to optimize their ion diffusion pathways and enhance their energy storage capabilities, thereby paving new ways for the development of high-performance electrochemical energy storage devices [51].

Herein, this work employs a facile microwave irradiation strategy to synthesize $Ag_6Mo_{10}O_{33}$ mesowires with a mean length of 14.71 μm, composed of numerous nanosheets with an average thickness of only 5 nm. Specifically, systematic investigations are carried out to explore the impact of reaction conditions on the shape of the products. The discovery of an innovative one-dimensional growth mechanism in nanomaterials, known as "self-assembly-dissolution-recrystallization-Ostwald-ripening" process, has been scientifically verified. Additionally, the electrochemical behavior of the ultralong and uniform $Ag_6Mo_{10}O_{33}$ mesowires in the Na^+ storage was investigated using various techniques. Notably, the $Ag_6Mo_{10}O_{33}$ mesowires exhibit an outstanding initial capacity of 1587.9 $mAh{\cdot}g^{-1}$ at 10 $mA{\cdot}g^{-1}$ and an excellent reversible capacity of 551.5 $mAh{\cdot}g^{-1}$ after 30 cycles. The presented research introduces a novel avenue for developing advanced silver molybdates electrode materials for high-capacity and stable energy storage.

2 Experimental

2.1 High-efficient synthesis of electrode materials

The $AgNO_3$ and $(NH_4)_6Mo_7O_{24}{\cdot}4H_2O$ were purchased from Shanghai Chemical Reagent Company (China) and Tianjin No. 4 Chemical Reagent Factory (China), respectively. Distilled water used for the chemical synthesis and evaluation experiments was deionized water collected from UKPRO ultrapure water system (China).

A series of parallel experiments were carried out to fabricate the $Ag_6Mo_{10}O_{33}$ meso/nanowires with diverse sizes and morphologies, through altering the vital fabricating conditions (such as the molar concentrations of raw materials and dwell time) as listed in the Table S1 in the Electronic Supplementary Material (ESM). All samples were prepared in a modified microwave irradiation reactor (Midea PJ21C-AU; power, 700 W; frequency, 2450 MHz) equipped with a water-cooled condenser in the refluxing system. The synthesis process can be described as follows: Initially, 0.50–4.00 mmol $AgNO_3$ and 0.07–0.57 mmol $(NH_4)_6Mo_7O_{24}{\cdot}4H_2O$ were dissolved in separate 10.0 mL solutions of distilled water in the 100 mL round-bottomed flask at room temperature. These solutions were then mixed and vigorously agitated for 10 min. The resultant mixture was transferred to a reaction vessel and heated to 100 °C for 2–120 min under microwave irradiation function. After the reaction concludes, the precipitates were cooled to ambient temperature, centrifuged at 9000 rpm for 30 min, washed repeatedly with distilled water, and dried in an oven at 60 °C for 24 h, yielding the meso/nanoscaled silver molybdate products [52].

2.2 Characterization

The X-ray diffraction (XRD) patterns of the as-synthesized silver molybdate were obtained using a D/MAX2500PC (Japan). Field emission scanning electron microscopy (FE-SEM) images were obtained using a Hitachi S-4800 (Japan) at an acceleration voltage of 10 kV to ascertain the shape and dimensions of the as-fabricated samples. Transmission electron microscopy (TEM) and high-resolution TEM (HRTEM) pictures were obtained using a Hitachi 7820 (Japan). The energy-dispersive X-ray (EDX) was validated using Bruker EDS QUANTAX XFlash 6TI30 equipment (Germany).

2.3 Electrochemical tests

The electrochemical measurements were conducted by assembling coin-type CR2032 cells in an Ar-filled glove box (MIKROUNA Universal, China, H_2O < 1 ppm, O_2 < 1 ppm). The slurry consisted

of 60 wt.% $Ag_6Mo_{10}O_{33}$, 30 wt.% carbon black (MMM Carbon, Brussels, Belgium), and 10 wt.% polyvinylidene fluoride (PVDF). The galvanostatic charge–discharge (GCD) curves were collected on a LAND CT2001A Battery Test System (Land, China) at room temperature (25 °C) with a voltage range from 0.02 to 3.50 V (vs. Li/Li^+).

3 Results and discussion

3.1 Rapid fabrication of $Ag_6Mo_{10}O_{33}$ meso/nanowire structures

Figure 1(a) exhibits the typical XRD pattern of the $Ag_6Mo_{10}O_{33}$ mesowires (Sample 1) that were treated under microwave irradiation process with the reaction time of 120 min, the $AgNO_3$ concentration of 0.300 mol·L^{-1} and the $(NH_4)_6Mo_7O_{24}$ concentration of 0.043 mol·L^{-1} as detailed in the Table S1 in the ESM. The strong and sharp reflection peaks are assigned to the pure phase of well-crystallized $Ag_6Mo_{10}O_{33}$ (ICDD-JCPDS card No. 72-1689, a = 7.950 Å, b = 8.310 Å, and c = 11.420 Å) [30]. Figure 1(b) affords valuable information regarding the crystalline structure of the material. Figures 1(c)–1(e) show representative FE-SEM images of as-fabricated $Ag_6Mo_{10}O_{33}$ at various magnifications, where bundles of superlong mesowires with a uniform morphology are successfully prepared under microwave irradiation process for 120 min. Figure 1(c) provides an overall view of the $Ag_6Mo_{10}O_{33}$ material composed of a large scale of relatively ultralong mesowires with approximately 290 nm in diameter (Fig. S1 in the ESM) and 14.71 μm in length (Fig. S9(d) in the ESM). The SEM pictures in Fig. 1(d) illustrate that these mesowires possess a highly organized structure and exceptionally smooth surfaces. The more amplified FE-SEM image in Fig. 1(e) confirms that these linear structures are composed of ultrathin nanosheets measuring about 5 nm in thickness (Fig. S4(d) in the ESM). Furthermore, TEM characterization was conducted to confirm the intricate microscale morphology and crystalline structure of $Ag_6Mo_{10}O_{33}$ mesowires. As shown in the Fig. 1(f), the uniform $Ag_6Mo_{10}O_{33}$ mesowires with a regular edge were observed. The HRTEM image shown in Fig. 1(h), which is an enlargement of the area marked by the yellow square in Fig. 1(g), reveals that the lattice spacing of $Ag_6Mo_{10}O_{33}$ is 0.422 nm,

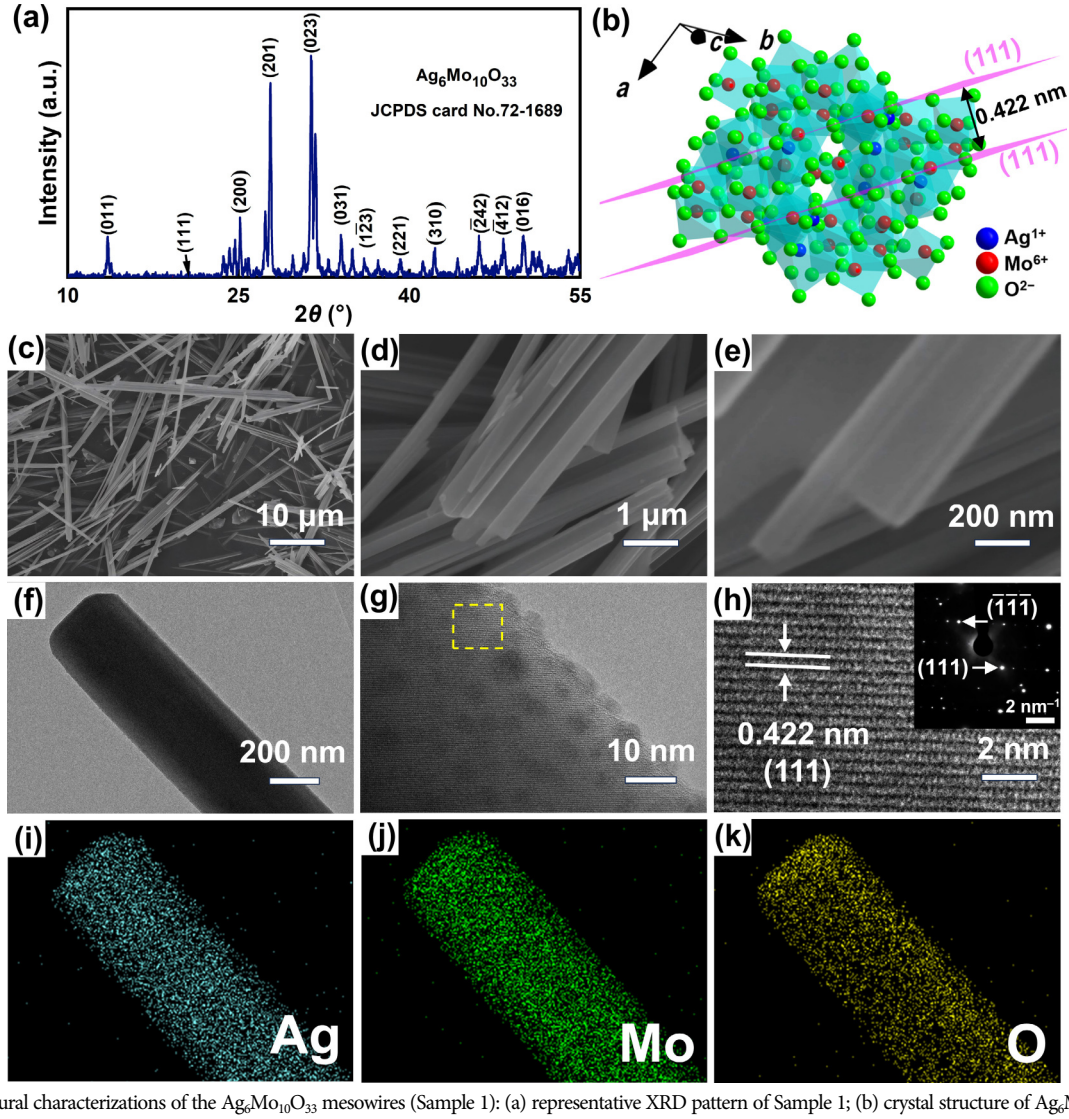

Figure 1 Structural characterizations of the $Ag_6Mo_{10}O_{33}$ mesowires (Sample 1): (a) representative XRD pattern of Sample 1; (b) crystal structure of $Ag_6Mo_{10}O_{33}$; ((c)–(e)) FE-SEM images of Sample 1; ((f) and (g)) TEM and HRTEM images of an individual $Ag_6Mo_{10}O_{33}$ mesowire; (h) expansion of the region within the yellow square in (g), and the inset in (h) displays the SAED pattern of $Ag_6Mo_{10}O_{33}$; ((i)–(k)) the elemental mappings of the single $Ag_6Mo_{10}O_{33}$ wire-like product.

corresponding to the adjacent (111) planes of $Ag_6Mo_{10}O_{33}$. The selected area electron diffraction (SAED) pattern, illustrated in the inset of Fig. 1(h), is employed to analyze and display the specific interplanar spacing of the (111) lattice plane, which is in a good agreement with the HRTEM image in Fig. 1(h). In addition, the elemental mappings depicted in Figs. 1(i)–1(k) show that Ag, Mo, and O elements are evenly distributed in the harvested $Ag_6Mo_{10}O_{33}$ mesowires, and no unexpected elements are detected, which fully confirms the purity of the as-fabricated product via the microwave irradiation strategy.

3.2 The exploration of reaction kinetics on $Ag_6Mo_{10}O_{33}$ meso/nanowires

To thoroughly explore the impact of the reaction kinetics on the shape and dimensions of as-obtained $Ag_6Mo_{10}O_{33}$ products, the concentration of $AgNO_3$ solution was tuned from 0.050 to 0.400 mol·L^{-1}, accompanied by corresponding changes in the concentration of $(NH_4)_6Mo_7O_{24}$ solution. Significant morphological alterations in the products, influenced by altering reactant concentrations, were distinctly identified through comprehensive investigation of FE-SEM images. Figures 2(a)–2(c) depict the FE-SEM images of the as-obtained granular $Ag_6Mo_{10}O_{33}$ aggregate microstructure (Sample 2: 0.050 mol·L^{-1}), characterized by a loose structure and rough surfaces, resembling particles of inconsistent size and appearance. The more amplified FE-SEM image in Fig. 2(b) demonstrates a restricted quantity of mesowires with diameters ranging from 110 to 260 nm (Fig. S6(a) in the ESM). Upon heightened magnification, several nanocones are observed on these aggregates, measuring around 33 nm in diameter and ranging from 194 to 305 nm in length (Fig. 2(c) and Figs. S3(a) and S3(b) in the ESM). As the reactant concentration rises to 0.200 mol·L^{-1} (Sample 3), the products evolve into monodisperse $Ag_6Mo_{10}O_{33}$ micro/nanoblocks, exhibiting a width of approximately 530 nm (Fig. S4(b) in the ESM) and lengths between 2.48 and 8.31 μm (Fig. S6(b) in the ESM), as illustrated in Figs. 2(d) and 2(e). In contrast to the $Ag_6Mo_{10}O_{33}$ derived from lower concentrations, these micro/nanorods demonstrate a standardized rod-shape and markedly improved surface flatness. Figure 2(f) illustrates that the $Ag_6Mo_{10}O_{33}$ nanorods are constructed by layering nanosheets with a thickness ranging from 5 to 9 nm (Fig. S4(a) in the ESM). When the concentration of $AgNO_3$ reached 0.400 mol·L^{-1} (Sample 4), the $Ag_6Mo_{10}O_{33}$ mesorods broke up into uneven fragments with an average width of 310 nm (Figs. 2(g) and 2(h) and Fig. S6(d) in the ESM). High magnification inspection (Fig. 2(i)) reveals that the surface nanosheets measure approximately 11 nm in thickness (Fig. S5(a) in the ESM). Compared with the previously mentioned parallel products, Sample 6 (0.300 mol·L^{-1}) exhibited well-defined mesowire structures and highly uniform morphological characteristics because of the enhanced nucleation rate and facilitated crystalline orientation growth achieved under efficient microwave irradiation function (Fig. S2 in the ESM). The $Ag_6Mo_{10}O_{33}$ nanorods break into uniformly sized radiating mesowires, leading to more prominent dimensions, specifically with a significantly reduced diameter (diameter: 165 nm, Fig. S6(c) in the ESM), thereby effectively increasing the specific surface area of the material. In summary, the morphology and size of the $Ag_6Mo_{10}O_{33}$ products exhibit considerable sensitivity to reactant concentration, with significant alterations in both form and structure. As the concentration gradually increases, the originally loosely structured aggregates become progressively more compact influenced by precipitation kinetics, with their surfaces transitioning from rough to smooth. However, excessively high concentrations significantly accelerate the reaction rate, resulting in decreased crystallinity and increased surface defects of the product, potentially causing the anticipated mesowire or mesorods morphology to transform into bulk structures or irregular shapes. Considering the aforementioned factors, subsequent experiments were conducted at the $AgNO_3$ concentration of 0.300 mol·L^{-1} to investigate the growth mechanism of $Ag_6Mo_{10}O_{33}$ meso/nanowires.

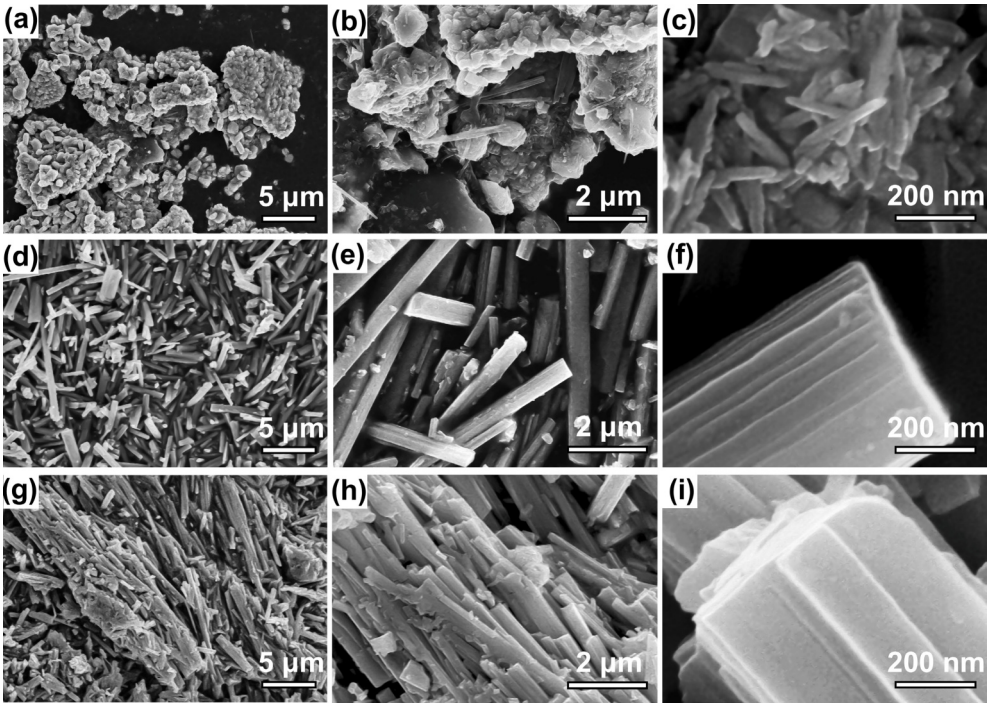

Figure 2 The corresponding FE-SEM images of $Ag_6Mo_{10}O_{33}$ synthesized at different concentrations of raw materials with a fixed molar ratio (Ag:Mo = 1:1) as summarized in the Table S1 in the ESM: ((a)–(c)) Sample 2; ((d)–(f)) Sample 3; ((g)–(i)) Sample 4.

To conduct in-depth insight of the actual growth mechanism of the ultralong meso/nanowire structure of $Ag_6Mo_{10}O_{33}$, under the $AgNO_3$ concentration of 0.300 mol·L^{-1} with the constant molar ratio (Ag:Mo = 1:1), XRD and FE-SEM techniques were utilized to observe the morphology of the products obtained at different reaction time ranging from 2 to 60 min (Samples 5–7), examining the influence of reaction time on the microstructure. Figure 3(a) displays the XRD patterns of as-fabricated $Ag_6Mo_{10}O_{33}$, where Samples 5–7 exhibit strong diffraction peaks at 11.125°, 26.621°, 29.746°, and 40.051°, corresponding to the JCPDS standard card (No. 72-1689). Notably, as indicated by Fig. 3(a)(1), high-purity $Ag_6Mo_{10}O_{33}$ materials were prepared using high-efficiency microwave irradiation technology within a reaction time of just 2 min. When focusing on the variation in reaction time for Samples 5–7 (from 2 to 60 min), the peaks of the $Ag_6Mo_{10}O_{33}$ phase at (101), (201), (023), and (031) gradually sharpen and increase in intensity, suggesting that the crystallinity of the samples improves as the reaction time extends. Additionally, as the reaction time continues to increase, the half-widths of these diffraction peaks corresponding to the Samples 5–7 also exhibit a gradual widening trend, further confirming an enhancement in the degree of nanoscale [50]. Subsequently, the structure and microtopography of the representative $Ag_6Mo_{10}O_{33}$ were meticulously analyzed by FE-SEM. At the sample synthesized for 2 min (Sample 5), the as-obtained $Ag_6Mo_{10}O_{33}$ exhibited structural features consisting of dense microclusters formed by the stacking of numerous smooth nanoflakes, measuring approximately 64 nm in thickness (Fig. S9(a) in the ESM) and 1.33 μm in length (Figs. 3(b)–3(d) and Fig. S10(a) in the ESM). As the microwave irradiation time was extended to 30 min (Sample 6), the low-magnification FE-SEM image (Fig. 3(e)) reveals that the radiating $Ag_6Mo_{10}O_{33}$ mesowires are concentrated on the surface of the microblock. These structures are consisted of a substantial quantity of nanowires bound tightly at the end, as illustrated in further detail in Fig. 3(f). Subsequently,

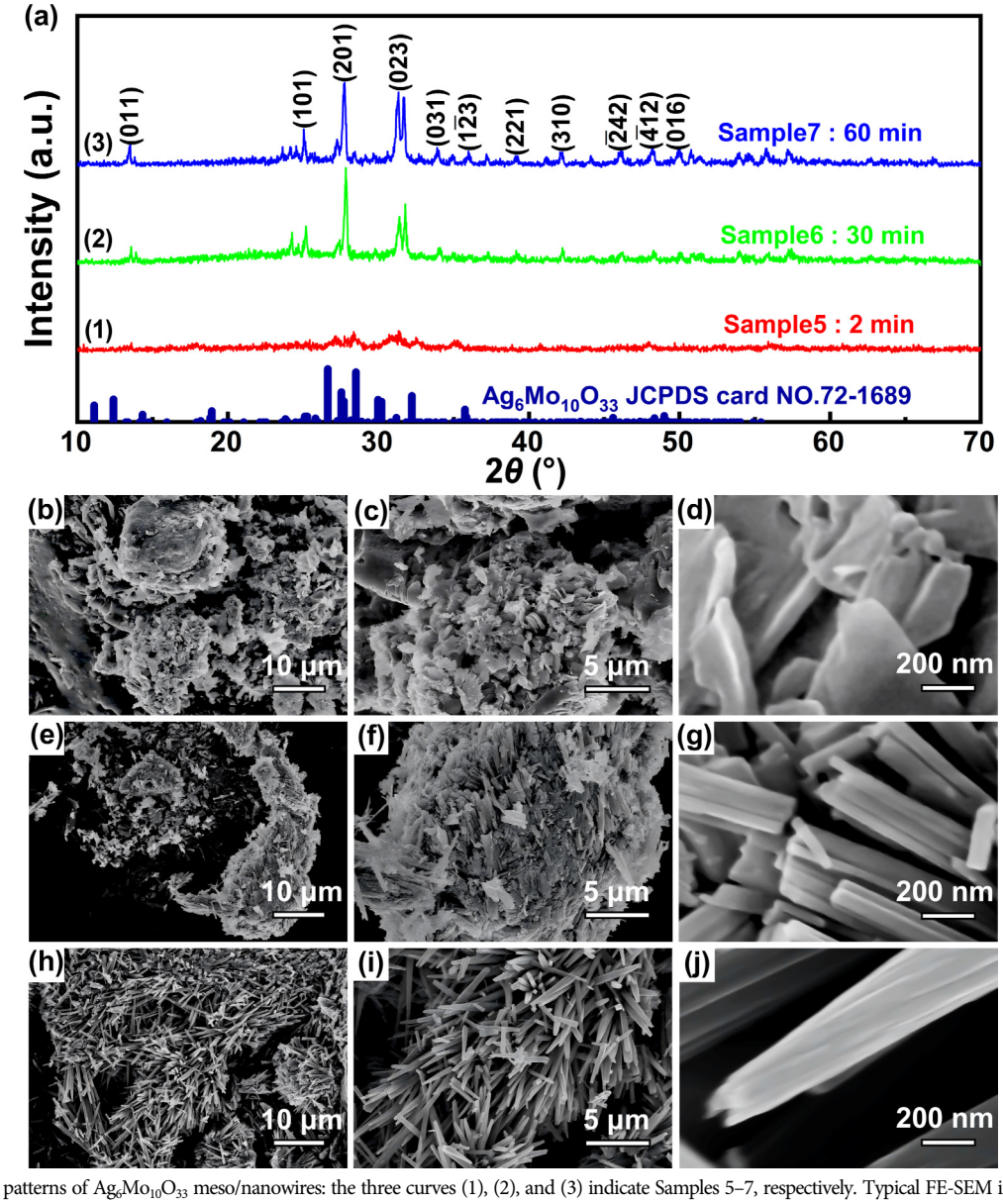

Figure 3 (a) XRD patterns of $Ag_6Mo_{10}O_{33}$ meso/nanowires: the three curves (1), (2), and (3) indicate Samples 5–7, respectively. Typical FE-SEM images of $Ag_6Mo_{10}O_{33}$ mesowires synthesized utilizing microwave irradiation at different reaction time: ((b)–(d)) Sample 5: 2 min, smooth nanoflakes; ((e)–(g)) Sample 6: 30 min, uniformly radiating mesowire; ((h)–(j)) Sample 7: 60 min, needle-like mesowires.

Fig. 3(g) confirms that the radiating nanowires exhibit relatively uniform morphology with a diameter of approximately 43 nm (Fig. S8 in the ESM) and lengths ranging from 1.00 to 3.00 μm (Fig. S10(b) in the ESM). As the heating time-span was prolonged to 60 min for Sample 7, needle-like $Ag_6Mo_{10}O_{33}$ mesowires (diameter: 0.58 μm, length: 5.15 μm, Figs. S10(c) and S13 in the ESM) emerged and exhibited radial organization characteristics at the micrometer scale, as shown in the Figs. 3(h) and 3(i). The needle-like $Ag_6Mo_{10}O_{33}$ mesowires are stacked with layers of ultrathin nanosheets with an average thickness of 6 nm (Fig. S9(c) in the ESM). Significantly, as depicted in Fig. 3(j), it was discovered that minor splitting and fusion phenomena occurred within the needle-like $Ag_6Mo_{10}O_{33}$ mesowires surface, indicating the ripening process is in progress. Ultimately, the morphologically consolidated $Ag_6Mo_{10}O_{33}$ mesowires were formed at 120 min through a ripening process. More notably, Sample 1 exhibits superior morphological characteristics, specifically represented as ultralong and ultrafine mesowires with a uniform distribution, as shown in Fig. S14 in the ESM. The advanced liner architecture of $Ag_6Mo_{10}O_{33}$ materials provides a high specific surface area and appropriate transport channels, facilitating the improvement of electrochemical performance. Under suitable reactant concentration conditions of 0.300 mol·L^{-1}, efficient microwave irradiation technology enabled the preparation of self-assembled $Ag_6Mo_{10}O_{33}$ materials within just 2 min of reaction time. Extending the reaction time to 30 min induced a dissolution-recrystallization process, leading to the initial formation of a mesowire structure. As the reaction time further increased, the mesowire size gradually expanded from 1.33 to 14.71 μm (Fig. S12 in the ESM), while the thickness of the thin sheets forming the mesowires decreased from 64 to 5 nm (Fig. S9 in the ESM). According to the above FE-SEM analysis, the morphologies of $Ag_6Mo_{10}O_{33}$ mesowires are extensively affected by the reaction time under the series conditions of highly efficient microwave irradiation function.

3.3 The growth mechanism of $Ag_6Mo_{10}O_{33}$ meso/nanowires

Based on the observed morphology evolution and phase transformation of Samples 5–7 and Sample 1 from 2 to 120 min, a possible fabricating mechanism of "self-assembly", "dissolution-recrystallization", and "Ostwald ripening" can be proposed to elucidate the formation process of superlong and homogeneous $Ag_6Mo_{10}O_{33}$ mesowires as illustrated in Fig. 4. In order to diminish surface energy during the first nucleation phase, many seeds began to arrange into $Ag_6Mo_{10}O_{33}$ nanofragments, which subsequently stacked into microscale clusters (Figs. 4(a) and 4(b)). The final crystal structure is heavily governed by the crystal growth phase of $Ag_6Mo_{10}O_{33}$, which is driven by a complex balance between kinetics and thermodynamics and benefits from microwave dielectric characteristics [53, 54]. As the reaction period extends, the inner $Ag_6Mo_{10}O_{33}$ nanofragments with high energy under high-temperature of microwave function were dissolved and recrystallized to form radialized $Ag_6Mo_{10}O_{33}$ mesowires with a larger diameter (Fig. 4(c)). Subsequently, the extensive growth of one-dimensional mesowires along the favored orientation, which leads to a consistent increase in length, predominantly depends on the progressive dissolution-recrystallization of irregular nanosheets. Eventually, it can be witnessed that the superlong and homogeneous $Ag_6Mo_{10}O_{33}$ mesowires were obtained, suggesting that these nanowires extend from the needle-like structure in a one-dimensional orientation (Figs. 4(d) and 4(e)), which corresponds with the established "Ostwald ripening" mechanism [55–58]. Significantly, the microwave irradiation provides a reliable method for fabricating and designing $Ag_6Mo_{10}O_{33}$ mesowires with high purity and a unique morphology. Evidently, the aforementioned formation mechanism plays a crucial role in the controlled synthesis of ultralong $Ag_6Mo_{10}O_{33}$ mesowires.

3.4 The electrochemical performances of the $Ag_6Mo_{10}O_{33}$ materials in SIBs

To evaluate the electrochemical properties of $Ag_6Mo_{10}O_{33}$ electrode materials, the coin-type cells were assembled using $Ag_6Mo_{10}O_{33}$ mesowires (Sample 1) as the working electrode and employing two kinds of collectors (Ti sheet and Al foil). The cyclic voltammetry (CV) curves (Figs. 5(a), 5(b), 5(d), and 5(e)) were collected at varying scan rates (30, 50, 70, and 100 mV·s^{-1}) within the potential range of −2.00 to 3.50 V to elucidate the reaction kinetics of $Ag_6Mo_{10}O_{33}$ electrode for the reversible Na^+ storage [55]. Figures 5(a) and 5(d) present the contour plots of the CV patterns for $Ag_6Mo_{10}O_{33}$ attached to the different collectors, respectively. The anodic peak at 1.00 V (Peak A) arises from the oxidation reaction in red region, whereas the cathodic peak at −0.50 V (Peak B) coincides with the reduction process in the blue region. Figures 5(b) and 5(e) illustrate the CV profiles corresponding to the contour plots. There is a pair of roughly symmetric redox peaks at 1.01 and −0.51 V, suggesting that the redox reactions of $Ag_6Mo_{10}O_{33}$ during charging and discharging exhibit a high electrochemical activity and reversibility. As the scanning rate increases, only minor shifts in peak positions are observed with no significant changes in peak shape. This phenomenon signifies that reversible electrochemical processes have transpired, further implying that the reaction kinetics are swift and the level of polarization is minimal. Additionally, the CV tests performed on Sample 1 mounted on Al foil demonstrated that the oxidation/reduction reaction potentials and profiles were markedly analogous to those recorded using Ti sheet as the current collector, suggesting a comparable sodium storage mechanism on both collectors. Figures 5(c) and 5(f) display the GCD profiles derived from 0.02 to 3.50 V (vs. Li^+/Li) at a current density of 10 mA·g^{-1}. In the first cycle, the electrodes for the Ti-sheet and Al-foil current collectors, deliver high initial discharge

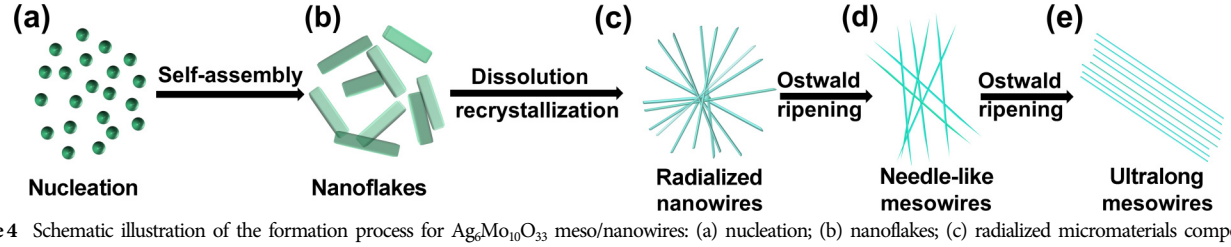

Figure 4 Schematic illustration of the formation process for $Ag_6Mo_{10}O_{33}$ meso/nanowires: (a) nucleation; (b) nanoflakes; (c) radialized micromaterials composed of nanowires; (d) needle-like mesowires; (e) ultralong mesowires.

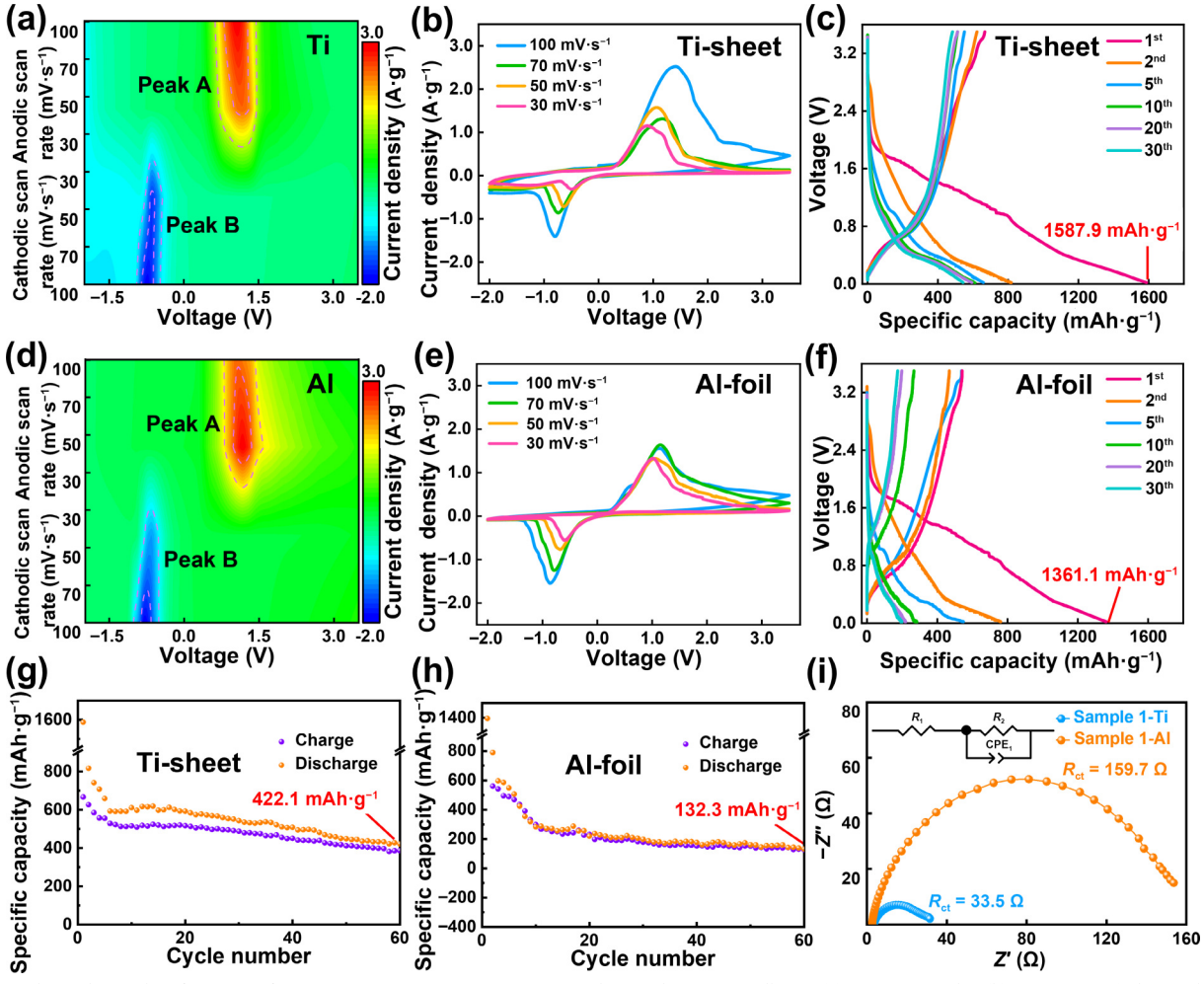

Figure 5 Electrochemical performance of $Ag_6Mo_{10}O_{33}$ mesowires in SIBs using Ti sheet as the current collector: (a) CV contour plot; (b) CV curves; (c) charge–discharge curves at a constant current density of 10 mA·g^{-1}; (g) cycling performance at 10 mA·g^{-1} for 60 cycles. Using Al foil as the current collector: (d) CV contour plot; (e) CV curves; (f) charge–discharge curves at a constant current density of 10 mA·g^{-1}; (h) cycling performance at 10 mA·g^{-1} for 60 cycles; (i) EIS plots of Sample 1 in SIBs utilizing Al-foil and Ti-sheet as current collectors.

capacities of 1587.9 and 1361.1 mAh·g^{-1}, respectively. This high capacity is indicative of the significant Na^+ storage capability of $Ag_6Mo_{10}O_{33}$ nanomaterials, driven by the unique structure. The high initial capacity also suggests that the material efficiently accommodates Na^+, rendering it a promising candidate for high-performance SIBs. After the initial cycle, the shape and voltage plateau of GCD curves consistently exhibited invariant, signifying highly reversible and stable electrochemical cycling performance (Figs. S15 and S16 in the ESM). However, a degree of capacity fading is observed in the subsequent cycles, which is commonly associated with the formation of a solid electrolyte interphase (SEI) layer and the irreversible trapping of Na^+ within the material [59, 60]. For the second cycle, the specific capacities decrease to around 817.9 in Ti and 759.5 mAh·g^{-1} in Al collector, which still remain significantly higher than that of the reported silver molybdate materials [61]. It is noted that the reversible capacity of the $Ag_6Mo_{10}O_{33}$ loaded on Ti sheet after 30 cycles of charging and discharging remained stable at 551.5 mAh·g^{-1}, maintaining 422.1 mAh·g^{-1} after 60 cycles, which demonstrates commendable cycling stability of the $Ag_6Mo_{10}O_{33}$ electrode (Fig. 5(g)). Regretfully, the capacity of $Ag_6Mo_{10}O_{33}$ using Al foil as collector fades to 198.7 mAh·g^{-1} after 30 cycles (Fig. 5(f)), followed by a decrease in capacity during the subsequent 30 cycles (60th cycle: 132.3 mAh·g^{-1}, Fig. 5(h)), which is relatively worse than that of $Ag_6Mo_{10}O_{33}$ loaded on Ti sheet. Based on the above analysis, besides the higher capacity, the $Ag_6Mo_{10}O_{33}$ attached to Ti-sheet also demonstrate a much better capacity retention than the $Ag_6Mo_{10}O_{33}$ load on Al foil. The electrochemical impedance spectroscopy (EIS) further verifies the above results (Fig. 5(i)). Comparing the electrochemical impedance of $Ag_6Mo_{10}O_{33}$ mesowires on various collectors revealed that the Al-foil electrode had higher resistance. It is possible that the relatively smooth surface of the Al foil results in inadequate bonding with the electrode material, leading to poor contact and consequently higher resistance, which further affects the electrochemical performances of the electrode [62, 63]. These results highlight the intrinsic stability of $Ag_6Mo_{10}O_{33}$ nanostructures as an electrode material, capable of sustaining high capacity over prolonged cycling, which is critical for practical battery applications.

4 Conclusion

In summary, ultralong $Ag_6Mo_{10}O_{33}$ mesowires with regular morphologies have been fabricated by the high-efficient microwave irradiation approach and investigated as electrochemical energy storage materials for SIBs. By meticulously controlling the reactant concentration and reaction duration, the ultralong $Ag_6Mo_{10}O_{33}$

mesowires, approximately 15.00 μm in length and composed of ultrathin nanosheets with an average thickness of 5 nm, were synthesized under the conditions of $AgNO_3$ concentration (0.300 mol·L^{-1}) with a fixed molar ratio (Ag:Mo = 1:1) and reaction time (120 min). Furthermore, the growth mechanism of ultralong and uniform $Ag_6Mo_{10}O_{33}$ mesowires was concluded into the "self-assembly-dissolution-recrystallization-Ostwald-ripening" process, based on the comparison of the phase and morphological evolutions of the $Ag_6Mo_{10}O_{33}$ materials obtained at various reaction time. Benefiting from the superior topology, $Ag_6Mo_{10}O_{33}$ mesowires exhibited an excellent initial specific capacity (1587.9 mAh·g^{-1}), a remarkable specific capacity for the second cycle (817.9 mAh·g^{-1}), and an outstanding reversible capacity after 60 cycles (422.1 mAh·g^{-1}). The proposed insights can provide better guidance for the morphology regulation of $Ag_6Mo_{10}O_{33}$ materials in frontier energy-related applications.

Electronic Supplementary Material: Supplementary material (the parallel experimental parameters and corresponding morphologies of the as-produced $Ag_6Mo_{10}O_{33}$ (Table S1); generalization of the experimental data and their structural information of the as-obtained $Ag_6Mo_{10}O_{33}$ nanowires (Figs. S1 and S3–S13); the SEM images of Samples 6 and 1 (Figs. S2 and S14); a table showing particle size and corresponding morphologies under different conditions (Table S2); the differential capacity (dQ/dV) curves corresponding to Figs. 5(c) and 5(f) (Figs. S15 and S16)) is available in the online version of this article at https://doi.org/10.26599/NR.2025.94907274.

Data availability

All data needed to support the conclusions in the paper are presented in the manuscript and the Electronic Supplementary Material. Additional data related to this paper may be requested from the corresponding author upon request.

Acknowledgements

This work was financially supported by the National Natural Science Foundation of China (No. 22379103), the Science and Technology Projects of Suzhou City (No. SYC2022043), the Qing Lan Project of Jiangsu Province (2022), Open Project of State Key Laboratory of Inorganic Synthesis and Preparative Chemistry (No. 2025-17), Hubei Key Laboratory of Energy Storage and Power Battery (Hubei University of Automotive Technology) (No. ZDK22023B01), and the Joint Funds of Advanced Functional Membrane Materials for the Natural Science Foundation of Anhui Province of China (No. 2408055UM003).

Declaration of competing interest

All the contributing authors report no conflict of interests in this work.

Author contribution statement

Y. Q. Y.: Investigation, data analysis, visualization, writing manuscript. J. L.: Investigation, methodology, data analysis, writing – review & editing. M. Q. Z.: Validation, resources. Q. W.: Software, investigation. Z. Q. G.: Methodology, visualization. C. S. L.: Methodology, project administration. Y. S.: Project administration, funding acquisition. X. C. G.: Methodology, data curation. Y. X. S.: Formal analysis. L. H. Q.: Investigation. Y. Z. Z.: Resources, validation. W. Z. L.: Validation. X. F. X.: Conceptualization, resources. X. F. W.: Conceptualization. All the authors have approved the final manuscript.

Use of AI statement

None.

References

[1] Qin, X.; Xu, B. L.; Lestas, I.; Guo, Y.; Sun, H. B. The role of electricity market design for energy storage in cost-efficient decarbonization. *Joule* **2023**, *7*, 1227–1240.

[2] Wang, Y. X.; Li, M.; Zhang, Y.; Zhang, N. Q. Hard carbon for sodium storage: Mechanism and performance optimization. *Nano Res.* **2024**, *17*, 6038–6057.

[3] Hou, S.; Ji, X.; Gaskell, K.; Wang, P. F.; Wang, L. N.; Xu, J. J.; Sun, R. M.; Borodin, O.; Wang, C. S. Solvation sheath reorganization enables divalent metal batteries with fast interfacial charge transfer kinetics. *Science* **2021**, *374*, 172–178.

[4] Sun, J.; Lee, H. W.; Pasta, M.; Yuan, H. T.; Zheng, G. Y.; Sun, Y. M.; Li, Y. Z.; Cui, Y. A phosphorene-graphene hybrid material as a high-capacity anode for sodium-ion batteries. *Nat. Nanotechnol.* **2015**, *10*, 980–985.

[5] Zhang, Q.; Gao, X. W.; Liu, X.; Mu, J. J.; Gu, Q. F.; Liu, Z. M.; Luo, W. B. Flexible wearable energy storage devices: Materials, structures, and applications. *Battery Energy* **2024**, *3*, 20230061.

[6] Xu, Z. W.; Song, K. W.; Chang, X. Y.; Li, L.; Zhang, W. C.; Xue, Y. X.; Zhang, J. H.; Lin, D. W.; Liu, Z. Y.; Wang, Q. et al. Layered oxide cathodes: A comprehensive review of characteristics, research, and development in lithium and sodium ion batteries. *Carbon Neutralization* **2024**, *3*, 832–856.

[7] Vaalma, C.; Buchholz, D.; Weil, M.; Passerini, S. A cost and resource analysis of sodium-ion batteries. *Nat. Rev. Mater.* **2018**, *3*, 18013.

[8] Gu, M. B.; Xu, J. L.; Shi, X. Y.; Shao, L. Y.; Sun, Z. P. Research progress of oxygen redox in sodium-layered oxides. *Battery Energy* **2024**, *3*, 20230046.

[9] Xing, B. Y.; Ren, J. K.; Hu, P.; Luo, W.; Mai, B.; Cai, H. W.; Wu, J. H.; Wu, X. F.; Chen, X. B.; Deng, Z. H. et al. Fluoride doping $Na_3Al_{2/3}V_{4/3}(PO_4)_3$ microspheres as cathode materials for sodium-ion batteries with multielectron redox. *Small* **2024**, *20*, 2310997.

[10] Zhang, L. P.; Li, X. L.; Yang, M. R.; Chen, W. H. High-safety separators for lithium-ion batteries and sodium-ion batteries: Advances and perspective. *Energy Storage Mater.* **2021**, *41*, 522–545.

[11] Guan, X.; Jian, Z. H.; Liao, X. A.; Liao, W. C.; Huang, Y. F.; Chen, D. Z.; Li, R. K. Y.; Liu, C. Tailored architecture of composite electrolyte for all-solid-state sodium batteries with superior rate performance and cycle life. *Nano Res.* **2024**, *17*, 4171–4180.

[12] Peng, B.; Zhou, Z. H.; Shi, J.; Xu, S.; Yang, J.; Xu, C. R.; Zuo, D. X.; Xu, J.; Ma, L. B.; Guo, S. H.; Zhou, H. S. A customized strategy realizes stable cycle of large-capacity and high-voltage layered cathode for sodium-ion batteries. *Angew. Chem., Int. Ed.* **2024**, *63*, e202411618.

[13] Wen, X.; Feng, W.; Li, X. H.; Yang, J. B.; Du, R. F.; Wang, P.; Li, H.; Song, L. Y.; Wang, Y. Z.; Cheng, M. et al. Diatomite-templated synthesis of single-atom cobalt-doped MoS_2/carbon composites to boost sodium storage. *Adv. Mater.* **2023**, *35*, 2211690.

[14] Yuan, T.; Fu, X. P.; Wang, Y.; Li, M. J.; Xia, S. X.; Pang, Y. P.; Zheng, S. Y. Enhanced conductivity and stability of Prussian blue cathodes in sodium-ion batteries by surface vapor-phase molecular self-assembly. *Nano Res.* **2024**, *17*, 4221–4230.

[15] Zhang, Y. X.; Chen, Y. Z. Y.; Jiang, Y.; Wang, J.; Zheng, X. Y.; Han, B.; Xia, K. S.; Gao, Q.; Cai, Z.; Zhou, C. G. et al. Construction of VS_2/VO_x heterostructure via hydrolysis-oxidation coupling reaction with superior sodium storage properties. *Adv. Funct. Mater.* **2023**, *33*,

2212785.
[16] Huang, S.; Sun, Y. Y.; Yuan, T.; Che, H. Y.; Zheng, Q. F.; Zhang, Y. X.; Li, P. Z.; Qiu, J.; Pang, Y. P.; Yang, J. H. et al. Mitigating voltage decay of O_3-$NaNi_{1/3}Fe_{1/3}Mn_{1/3}O_2$ layered oxide cathode for sodium-ion batteries by incorporation of 5D metal tantalum. *Carbon Neutralization* **2024**, *3*, 584–596.
[17] Liu, Q. N.; Hu, Z.; Chen, M. Z.; Zou, C.; Jin, H. L.; Wang, S.; Chou, S. L.; Liu, Y.; Dou, S. X. The cathode choice for commercialization of sodium-ion batteries: Layered transition metal oxides versus Prussian blue analogs. *Adv. Funct. Mater.* **2020**, *30*, 1909530.
[18] Liu, Q. N.; Hu, Z.; Li, W. J.; Zou, C.; Jin, H. L.; Wang, S.; Chou, S. L.; Dou, S. X. Sodium transition metal oxides: The preferred cathode choice for future sodium-ion batteries. *Energy Environ. Sci.* **2021**, *14*, 158–179.
[19] Tan, M. D.; Han, S. H.; Li, Z. B.; Cui, H.; Lei, D. N.; Wang, C. X. Compact Sn/C composite realizes long-life sodium-ion batteries. *Nano Res.* **2023**, *16*, 3804–3813.
[20] Sharipova, A.; Klinger, L.; Bisht, A.; Straumal, B. B.; Rabkin, E. Solid-state dewetting of thin Au films on oxidized surface of biomedical TiAlV alloy. *Acta Mater.* **2022**, *231*, 117919.
[21] Fan, H. N.; Zhang, Q.; Gu, Q. F.; Li, Y.; Luo, W. B.; Liu, H. K. Exploration of the sodium ion ordered transfer mechanism in a $MoSe_2$@graphene composite for superior rate and lifespan performance. *J. Mater. Chem. A* **2019**, *7*, 13736–13742.
[22] Xu, J.; Jiang, J. B.; Cao, S. F.; Li, S. W.; Ma, Y. M.; Chen, J. W.; Zhang, Y.; Lu, X. Q. Amorphous carbon intercalated MoS_2 nanosheets embedded on reduced graphene oxide for excellent high-rate and ultralong cycling sodium storage. *EcoMat* **2024**, *6*, e12479.
[23] Zhou, J.; Hu, H. Y.; Li, H. Q.; Chen, Z. P.; Yuan, C. Z.; He, X. J. Advanced carbon-based materials for Na, K, and Zn ion hybrid capacitors. *Rare Met.* **2023**, *42*, 719–739.
[24] Suntharam, N. M.; Bashir, S.; Vengadaesvaran, B.; Rahim, N. A.; Reasmyraj, S.; Ramesh, S.; Ramesh, K.; Prasankumar, T. Fundamentals and key components of sodium-ion batteries: Challenges and future perspectives. *Mater. Today Chem.* **2024**, *42*, 102350.
[25] Santhoshkumar, P.; Vikraman, D.; Hussain, S.; Karuppasamy, K.; Kathalingam, A.; Kim, H. S. 3D-architectured spherical $Ce_2Mo_5O_{16}$ by a time-dependent hydrothermal process and their energy storage application. *J. Alloys Compd.* **2022**, *928*, 167215.
[26] Hu, J. X.; Xie, Y. Y.; Zheng, J. Q.; Lai, Y. Q.; Zhang, Z. A. Unveiling nanoplates-assembled Bi_2MoO_6 microsphere as a novel anode material for high performance potassium-ion batteries. *Nano Res.* **2020**, *13*, 2650–2657.
[27] Suresh Babu, G.; Shakkeel, N. K.; Kalaiselvi, N. $FeMoO_4$ nanorods anchored on graphene sheets as a potential anode for high performance sodium ion batteries. *J. Alloys Compd.* **2021**, *877*, 160306.
[28] Wang, D. D.; Li, C. S.; Yang, C.; Sun, Y.; Peng, W. X.; Dai, G. L.; Zhao, Y. J.; Liu, P. C.; Wang, L. N.; Zhao, Y. Z. et al. $CaMoO_4$ Persimmon/MCMB composites with highly exposed (103) active facets and enhanced properties for reversible lithium storage. *Compos. Part B Eng.* **2022**, *247*, 110301.
[29] Zhang, J. L.; Ma, Z. $Ag_6Mo_{10}O_{33}$/g-C_3N_4 1D–2D hybridized heterojunction as an efficient visible-light-driven photocatalyst. *Mol. Catal.* **2017**, *432*, 285–291.
[30] Misra, S.; Sahoo, S.; Jayaraman, V.; Arora, A. K.; Gnanasekaran, T. Effect of annealing on microstructure and phase evolution of $Ag_6Mo_{10}O_{33}$ nanorods synthesised by novel soft chemical method. *Int. J. Nanotechnol.* **2010**, *7*, 870–882.
[31] Prabhu, E.; Madhavan, R. R.; Jayaraman, V.; Gnanasekar, K. I. Selective response of $Ag_6Mo_{10}O_{33}$ thick film toward ammonia using AC measurement. *J. Electrochem. Soc.* **2019**, *166*, B1196–B1201.
[32] Moura, J. V. B.; Freitas, T. S.; Cruz, R. P.; Pereira, R. L. S.; Silva, A. R. P.; Santos, A. T. L.; da Silva, J. H.; Luz-Lima, C.; Freire, P. T. C.; Coutinho, H. D. M. β-Ag_2MoO_4 microcrystals: Characterization, antibacterial properties and modulation analysis of antibiotic activity. *Biomed. Pharmacother.* **2017**, *86*, 242–247.
[33] Della Rocca, R. D.; Victória, H. F. V.; Moura-Nickel, C. D.; Scaratti, G.; Krambrock, K.; De Noni, A.; Vilar, V. J. P.; José, H. J.; Moreira, R. F. P. M. Peroxidation and photo-peroxidation of pantoprazole in aqueous solution using silver molybdate as catalyst. *Chemosphere* **2021**, *262*, 127671.
[34] Guo, H.; Xie, J. W.; He, G. Z.; Zhu, D. Z.; Qiao, M.; Yan, J. F.; Yu, J. C.; Li, J. Q.; Zhao, Y. Z.; Luo, M. et al. A review of ultrafast laser micro/nano fabrication: Material processing, surface/interface controlling, and devices fabrication. *Nano Res.* **2024**, *17*, 6212–6230.
[35] Li, C. S.; Cheng, F. Y.; Ji, W. Q.; Tao, Z. L.; Chen, J. Magnesium microspheres and nanospheres: Morphology-controlled synthesis and application in Mg/MnO_2 batteries. *Nano Res.* **2009**, *2*, 713–721.
[36] Chen, Y.; Zhang, X. Y.; Jiang, J. Z.; Chen, G. Y.; Zhou, K. H.; Zhang, X. W.; Li, F. J.; Yuan, C. J.; Bao, J. C.; Xu, X. X. Microfluidic synthesis of hollow $CsPbBr_3$ perovskite nanocrystals through the nanoscale Kirkendall effect. *Nano Res.* **2024**, *17*, 8487–8494.
[37] Lin, C. J.; Zhang, J. T.; von Lim, Y.; Yan, D.; Li, K.; Leong, Z. Y.; Vafakhah, S.; Li, Y. F.; Silva, A.; Yang, H. Y. 3D hierarchical architectures of $CoSe_2$ nanoparticles embedded in rice-derived hard carbon for advanced sodium storage. *Carbon Neutralization* **2022**, *1*, 224–232.
[38] Sun, Y.; Li, C. S.; Yang, Q. R.; Chou, S. L.; Liu, H. K. Electrochemically active, novel layered *m*-ZnV_2O_6 nanobelts for highly rechargeable Na-ion energy storage. *Electrochim. Acta* **2016**, *205*, 62–69.
[39] Wang, F.; Jiang, Z. M.; Zhang, Y. Y.; Zhang, Y. L.; Li, J. D.; Wang, H. B.; Jiang, Y. Z.; Xing, G. C.; Liu, H. C.; Tang, Y. X. Revitalizing sodium-ion batteries via controllable microstructures and advanced electrolytes for hard carbon. *eScience* **2024**, *4*, 100181.
[40] Yuan, T.; Li, P. Z.; Sun, Y. Y.; Che, H. Y.; Zheng, Q. F.; Zhang, Y. X.; Huang, S.; Qiu, J.; Pang, Y. P.; Yang, J. H. et al. Refining O_3-type Ni/Mn-based sodium-ion battery cathodes via "atomic knife" achieving high capacity and stability. *Adv. Funct. Mater.* **2025**, *35*, 2414627.
[41] Montenegro, J. E.; Villalobos, C. M.; Singh, D. P. Ethylene glycol mediated facile and controlled growth of ultralong hexagonal silver molybdate microrods. *Mater. Lett.* **2018**, *215*, 129–133.
[42] Zhou, P.; Wang, L. P.; Zhang, M. Y.; Huang, Q. Z.; Su, Z. A.; Wang, X. D.; Guo, D. R.; Liao, M. D.; Xu, P.; Lin, X. B. Hierarchical structural modulation and Co-construction of selenium vacancy in ZnSe/$NiSe_2$ heterojunctions to enhance cycling stability and fast ion diffusion kinetics for lithium-ion and sodium-ion batteries. *Chem. Eng. J.* **2024**, *488*, 150829.
[43] Song, Z. Q.; Di, M. X.; Zhang, X. Y.; Wang, Z. Y.; Chen, S. H.; Zhang, Q. Y.; Bai, Y. Nanoconfined strategy optimizing hard carbon for robust sodium storage. *Adv. Energy Mater.* **2024**, *14*, 2401763.
[44] Safartoobi, A.; Mazloom, J.; Ghodsi, F. E. Silver/molybdenum metal-organic framework derived Ag_2MoO_4 nanoparticles as novel electrode for high-performance supercapacitor. *J. Energy Storage* **2023**, *68*, 107818.
[45] Chen, N.; Gao, Y.; Zhang, M. N.; Meng, X.; Wang, C. Z.; Wei, Y. J.; Du, F.; Chen, G. Electrochemical properties and sodium-storage mechanism of $Ag_2Mo_2O_7$ as the anode material for sodium-ion batteries. *Chem.—Eur. J.* **2016**, *22*, 7248–7254.
[46] Fabbro, M. T.; Saliby, C.; Rios, L. R.; La Porta, F. A.; Gracia, L.; Li, M. S.; Andrés, J.; Santos, L. P. S.; Longo, E. Identifying and rationalizing the morphological, structural, and optical properties of β-Ag_2MoO_4 microcrystals, and the formation process of Ag nanoparticles on their surfaces: Combining experimental data and first-principles calculations. *Sci. Technol. Adv. Mater.* **2015**, *16*, 065002.
[47] Anderegg, L.; Burchesky, S.; Bao, Y. C.; Yu, S. S.; Karman, T.; Chae, E.; Ni, K. K.; Ketterle, W.; Doyle, J. M. Observation of microwave shielding of ultracold molecules. *Science* **2021**, *373*, 779–782.
[48] Chen, J. W.; Adit, G.; Li, L.; Zhang, Y. X.; Chua, D. H. C.; Lee, P. S. Optimization strategies toward functional sodium-ion batteries. *Energy Environ. Mater.* **2023**, *6*, e12633.
[49] Zhou, Y. F.; Lin, F. W.; Ling, Z. Q.; Zhan, M. X.; Zhang, G. X.;

Yuan, D. K. Comparative study by microwave pyrolysis and conventional pyrolysis of pharmaceutical sludge: Resourceful disposal and antibiotic adsorption. *J. Hazard. Mater.* **2024**, *468*, 133867.

[50] Zhu, J. H.; Li, C. S.; Sun, Y.; Yang, C.; Zhao, Y. J.; Zhu, Z.; Wang, D. D.; Hu, Z.; Chou, S. L.; Li, L. et al. Enhanced photoluminescence of hollow $CaWO_4$ microspheres: The fast fabrication, structural manipulation, and exploration of the growth mechanism. *Mater. Chem. Front.* **2022**, *6*, 1046–1055.

[51] Li, C. S.; Sun, Y.; Ma, X. G.; Yao, W. X.; Hu, Y. W.; Wang, Y. D.; Wang, Y. Z. Ultralong triclinic-$Ba_2V_2O_7$ nanowires: Microwave radiation-assisted CTAB surfactant synthesis, the novel growth mechanism and optical activity performances. *RSC Adv.* **2014**, *4*, 9737–9742.

[52] Tao, X.; Wei, M. Q.; Yu, L. H.; Zhuang, B. C.; Zhang, L. L.; Zhu, R. L.; Zhao, G. Z.; Han, L.; Zhu, Y. Y.; Jin, H. L. et al. Facile microwave-assisted synthesis of Ce-doped Bi_2O_3 for efficient hybrid supercapacitors. *Battery Energy* **2024**, *3*, 20230052.

[53] Wang, W. Q.; Qiao, Z. J.; Zhao, Y. W.; Xie, G.; Yan, S. L.; Pang, Z. H.; Chen, Y. F.; Yang, H.; Zhang, M. M.; Zhang, Y. F. et al. SO_4^{2-}-ion induced synthesis of 3D porous hydrangea-shaped anatase TiO_2 as high performance anode material for lithium/sodium-ion batteries. *J. Porous Mater.* **2023**, *30*, 1245–1253.

[54] Sun, Y.; Li, C. S.; Wang, L. N.; Wang, Y. Z.; Ma, X. G.; Ma, P. J.; Song, M. Y. Ultralong monoclinic ZnV_2O_6 nanowires: Their shape-controlled synthesis, new growth mechanism, and highly reversible lithium storage in lithium-ion batteries. *RSC Adv.* **2012**, *2*, 8110–8115.

[55] Lee, H. J.; Oh, S.; Cho, K. Y.; Jeong, W. L.; Lee, D. S.; Park, S. J. Spontaneous and selective nanowelding of silver nanowires by electrochemical Ostwald ripening and high electrostatic potential at the junctions for high-performance stretchable transparent electrodes. *ACS Appl. Mater. Interfaces* **2018**, *10*, 14124–14131.

[56] Lee, H. J.; Yang, U. J.; Kim, K. N.; Park, S.; Kil, K. H.; Kim, J. S.; Wodtke, A. M.; Choi, W. J.; Kim, M. H.; Baik, J. M. Directional Ostwald ripening for producing aligned arrays of nanowires. *Nano Lett.* **2019**, *19*, 4306–4313.

[57] Lotty, O.; Hobbs, R.; O'Regan, C.; Hlina, J.; Marschner, C.; O' Dwyer, C.; Petkov, N.; Holmes, J. D. Self-seeded growth of germanium nanowires: Coalescence and Ostwald ripening. *Chem. Mater.* **2013**, *25*, 215–222.

[58] Liu, C. H.; Li, R. T.; Fan, Y. M.; Li, S. W.; Feng, X. H.; Feng, L.; Ning, Y. X.; Fu, Q. Liquid-mediated Ostwald ripening of Ag-based clusters supported on oxides. *Nano Res.* **2024**, *17*, 4971–4978.

[59] Yang, A. K.; Yao, K.; Schaller, M.; Dashjav, E.; Li, H.; Zhao, S.; Zhang, Q.; Etter, M.; Shen, X. C.; Song, H. M. et al. Enhanced room-temperature Na^+ ionic conductivity in $Na_{4.92}Y_{0.92}Zr_{0.08}Si_4O_{12}$. *eScience* **2023**, *3*, 100175.

[60] Chen, D. Q.; Hu, C. J.; Chen, Q.; Xue, G. Y.; Tang, L. F.; Dong, Q. Y.; Chen, B. W.; Zhang, F. R.; Gao, M. W.; Xu, J. J. et al. High ceramic content composite solid-state electrolyte films prepared via a scalable solvent-free process. *Nano Res.* **2023**, *16*, 3847–3854.

[61] Li, C. S.; Zhang, S. Y.; Cheng, F. Y.; Ji, W. Q.; Chen, J. Porous $LiFePO_4$/NiP Composite nanospheres as the cathode materials in rechargeable lithium-ion batteries. *Nano Res.* **2008**, *1*, 242–248.

[62] Liu, S.; Tang, S.; Zhang, X. Y.; Wang, A. X.; Yang, Q. H.; Luo, J. Y. Porous Al current collector for dendrite-free Na metal anodes. *Nano Lett.* **2017**, *17*, 5862–5868.

[63] Wu, H.; Song, Z. Y.; Wang, X. X.; Feng, W. F.; Zhou, Z. B.; Zhang, H. N,N-dimethyl fluorosulfonamide for suppressed aluminum corrosion in lithium bis(trifluoromethanesulfonyl)imide-based electrolytes. *Nano Res.* **2023**, *16*, 8269–8280.